

# Hydrazine Hydrate Intercalated 1T-Dominant MoS<sub>2</sub> with Superior Ambient Stability for Highly Efficient Electrocatalytic Applications

Mengyao Li, Zizhen Zhou, Long Hu, Shuangyue Wang, Yingze Zhou, Renbo Zhu, Xueze Chu, Ajayan Vinu, Tao Wan,\* Claudio Cazorla,\* Jiabao Yi,\* and Dewei Chu



Cite This: *ACS Appl. Mater. Interfaces* 2022, 14, 16338–16347



Read Online

ACCESS |



Metrics & More



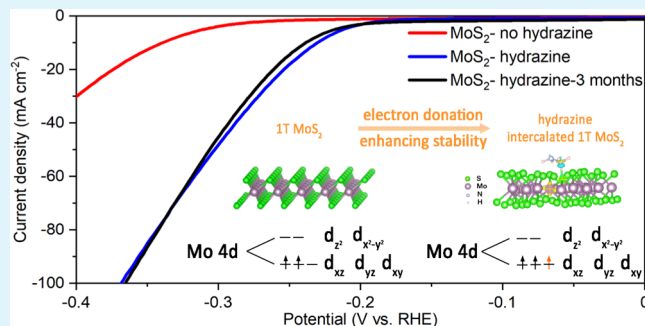
Article Recommendations



Supporting Information

**ABSTRACT:** Metallic 1T-phase MoS<sub>2</sub> exhibits superior hydrogen evolution reaction (HER) performance than natural 2H-phase MoS<sub>2</sub> owing to its higher electrical conductivity and abundance of active sites. However, the reported 1T-MoS<sub>2</sub> catalysts usually suffer from extreme instability, which results in quick phase transformation at ambient conditions. Herein, we present a facile approach to engineer the phase of MoS<sub>2</sub> by introducing intercalated hydrazine. Interestingly, the as-synthesized 1T-dominant MoS<sub>2</sub> sample demonstrates excellent ambient stability without noticeable degradation for 3 months. Additionally, the 1T-dominant MoS<sub>2</sub> exhibits superior electrical conductivity (~700 times higher than that of 2H-MoS<sub>2</sub>) and improved electrochemical catalytic performance (current density ~12 times larger than that of 2H-MoS<sub>2</sub> at an overpotential of 300 mV vs the reversible hydrogen electrode, RHE). Through experimental characterizations and density functional theory (DFT) calculation, we conclude that the stabilization of the metallic phase could be attributed to the electron donation from hydrazine molecules to the adjacent Mo atoms. The phase control strategy in this work provides a guideline to develop other highly efficient and stable two-dimensional (2D) electrocatalysts.

**KEYWORDS:** 2D transition metal dichalcogenides, hydrogen evolution reaction, phase stability, hydrazine intercalation, density functional theory



of 2H-MoS<sub>2</sub> at an overpotential of 300 mV vs the reversible hydrogen electrode, RHE). Through experimental characterizations and density functional theory (DFT) calculation, we conclude that the stabilization of the metallic phase could be attributed to the electron donation from hydrazine molecules to the adjacent Mo atoms. The phase control strategy in this work provides a guideline to develop other highly efficient and stable two-dimensional (2D) electrocatalysts.

potentials of 200–300 mV and Tafel slopes of 80–120 mV/dec.<sup>15,16</sup> Meanwhile, the metallic 1T phase is increasingly drawing more attention owing to its unique symmetry (octahedral prismatic coordination) and promising catalytic properties,<sup>17</sup> comparable to the other non-noble metal-based electrocatalysts.<sup>18,19</sup> It has been reported that the basal plane of 1T-MoS<sub>2</sub> displays excellent electrical conductivity and favorable H<sub>2</sub> binding energy, thus boosting the HER process resulting from its abundant active sites and fast electron transfer rate.<sup>20,21</sup> In contrast to the unsatisfactory HER performance of 2H-MoS<sub>2</sub>, 1T-MoS<sub>2</sub> exhibits low onset potentials of 100–200 mV and reduced Tafel slopes of 40–80 mV/dec.<sup>22,23</sup> Additionally, the catalytic property of 1T-MoS<sub>2</sub> could be further enhanced through strategies such as element doping,<sup>24</sup> strain engineering,<sup>25</sup> interface modulation,<sup>26</sup>

## 1. INTRODUCTION

Molybdenum disulfide (MoS<sub>2</sub>), a typical transition metal dichalcogenide (TMD) with a layered structure, has been widely studied owing to its unique electrical,<sup>1</sup> optical,<sup>2</sup> mechanical,<sup>3</sup> magnetic,<sup>4</sup> and catalytic properties.<sup>5,6</sup> In general, the molybdenum atoms are covalently bonded with two adjacent sulfur atoms to form a single layer of MoS<sub>2</sub>, which are stacked with each other via weak van der Waals forces to form bulk layered materials. This unique structural unit appears in several MoS<sub>2</sub> polymorphs, such as 1T (1T'),<sup>7,8</sup> 2H,<sup>9</sup> and 3R<sup>10</sup> phases, which may present quite different physical properties. Natural MoS<sub>2</sub> exists in a thermally stable semiconductive 2H phase (trigonal prismatic coordination) that has been extensively applied in many fields, including solid lubricants,<sup>3</sup> field-effect transistors (FETs),<sup>1</sup> biosensors,<sup>11</sup> and optical sensors.<sup>2</sup>

However, this most stable MoS<sub>2</sub> phase has a limited number of edge Mo ions as active sites, which is unfavorable for catalyzing the hydrogen evolution reaction (HER).<sup>12,13</sup> Moreover, the catalytic property of 2H-MoS<sub>2</sub> is further limited by its poor electrical conductivity and unsuitable hydrogen molecule binding.<sup>14</sup> Consequently, 2H-MoS<sub>2</sub> usually exhibits unsatisfactory catalysis performance with too high onset

**Received:** February 13, 2022

**Accepted:** March 21, 2022

**Published:** April 1, 2022



and defects engineering.<sup>27</sup> Therefore, 1T-MoS<sub>2</sub> has been considered as an excellent candidate for HER applications.

Currently, the common strategies to synthesize 1T phase of MoS<sub>2</sub> involve metal ions (Li<sup>+</sup>, K<sup>+</sup>, etc.) intercalation,<sup>28</sup> covalent functionalization,<sup>29</sup> water-coupled electron doping,<sup>30</sup> Mo substitution (e.g., by Re and Mn),<sup>31</sup> and molten-metal-assisted intercalation.<sup>32</sup> In the abovementioned strategies, the foreign species serve as electron donors. However, the 1T-MoS<sub>2</sub> samples synthesized using the above methods typically suffer from thermodynamical instability due to their relatively high energy configuration, which leads to gradual or quick transformation from the 1T to the 2H phase at room temperature (i.e., within a time window of 2 h).<sup>33,34</sup> Specifically, MoS<sub>2</sub> presents the largest 1T–2H energy difference among the VI group TMDs;<sup>35</sup> hence it is particularly difficult to obtain stable 1T-MoS<sub>2</sub>. In addition, conventional synthesis of 1T-MoS<sub>2</sub> (e.g., through chemical exfoliation) is time-consuming and the resulting nanostructure morphology can be easily impaired during the intercalation process.<sup>22</sup> Therefore, it remains challenging to synthesize 1T-MoS<sub>2</sub> via a facile strategy able to preserve its excellent catalytical properties and simultaneously ensure long-term stability at ambient conditions.

In this work, we present a one-step hydrazine-assisted hydrothermal method to synthesize 1T-phase-dominant MoS<sub>2</sub> nanosheets. By simply tuning the amount of the hydrazine precursor, the ratio of the 2H/1T phase can be continuously modulated. Our research shows that upon increasing the 1T/2H ratio, the electrical conductivity of MoS<sub>2</sub> is significantly improved and the electrochemical HER catalytic performance is drastically enhanced (i.e., the Tafel slope decreases from 99 to 64 mV/dec). More importantly, the as-prepared 1T-phase-dominant MoS<sub>2</sub> exhibits outstanding stability at room temperature without noticeable phase transformation occurring for 3 months. Furthermore, density functional theory (DFT) analysis reveals that the interactions between the N<sub>2</sub>H<sub>4</sub> molecules in the hydrazine precursor and MoS<sub>2</sub> are only favorable for the 1T polymorph (i.e.,  $E_{\text{intercalation}} < 0$ ), which may explain its enhanced thermal stability in terms of the reduction of Mo ions driven by hydrazine electron donation. Therefore, the effective 1T-MoS<sub>2</sub> stabilization method introduced in this work is likely to boost the use of TMD-layered materials in electrocatalytic applications as well as in other technological fields.

## 2. EXPERIMENTAL SECTION

**2.1. Material Preparation.** All of the chemicals were purchased from Sigma-Aldrich. Graphite paper was purchased from Beijing Jinglong Special Carbon (0.5 mm thick). All of the MoS<sub>2</sub> samples were synthesized by a hydrothermal method. In detail, 0.53 g × 4 of ammonium heptamolybdate [(NH<sub>4</sub>)<sub>6</sub>Mo<sub>7</sub>O<sub>24</sub>·4H<sub>2</sub>O] as Mo source and 0.46 g × 4 of TAA (C<sub>2</sub>H<sub>3</sub>NS) as S source were put into four beakers. Hydrazine monohydrate (N<sub>2</sub>H<sub>4</sub>·H<sub>2</sub>O) in volumes of 0, 0.15, 0.58, and 1.75 mL was dissolved in each beaker to make the molar ratio of N<sub>2</sub>H<sub>4</sub>/Mo 0:1, 1:1, 4:1, and 12:1, respectively. Then, deionized (DI) water was added to make the mixture volume 40 mL, and the whole set was continuously stirred for 1 h. Then, the precursors were transferred to four clean 50 mL stainless-steel autoclaves and put in the oven at 180 °C for 48 h. After cooling down to room temperature, the suspension was taken out and washed with DI water and ethanol at least five times. The final product was vacuum-dried in an oven at 50 °C for 6 h, and we obtained the black loose powder labeled as samples MoS<sub>2</sub>-0HZ, MoS<sub>2</sub>-1HZ, MoS<sub>2</sub>-4HZ, and MoS<sub>2</sub>-12HZ. The comparison samples MoS<sub>2</sub>-0HZ-220 and MoS<sub>2</sub>-4HZ-220 were prepared by a similar method with a higher

hydrothermal temperature at 220 °C. A part of the MoS<sub>2</sub>-4HZ powder was stored at room temperature for 3 months and labeled as MoS<sub>2</sub>-4HZ-3M.

**2.2. Material Characterization.** The morphology and atomic structure were characterized by scanning electron microscopy (SEM, FEI Nova NanoSEM 450) and transmission electron microscopy (TEM, JEOL JEM-F200 Multi-Purpose FEG-S/TEM) equipped with an energy-dispersive spectroscopy detector (EDS, Bruker SDD-EDS detector). X-ray diffraction (XRD) measurement was recorded with an MPD (PANalytical) Xpert Multipurpose X-ray Diffraction System with Cu K $\alpha$  radiation. Raman spectra were measured by a Renishaw inVia Raman Microscope, excited with a 532 nm wavelength argon-ion laser. Raman spectroscopy was calibrated with a Si single crystal before measurement. The composition and chemical bonding were analyzed by ThermoScientific ESCALAB 250i X-ray photoelectron spectroscopy (XPS). The binding energies were calibrated by the C 1s peak at 284.86 eV.

**2.3. Electrochemical Measurements.** The electrochemical measurements were carried out with a three-electrode cell on an electrochemical workstation (Autolab PGSTAT302N). The working electrode was prepared by loading the sample powders on a graphite paper. Five milligrams of powder was dispersed into 1.0 mL of mixed solution (490  $\mu$ L of DI water, 490  $\mu$ L of ethanal, and 20  $\mu$ L of 5 wt % Nafion). The mixture was ultrasonicated for 2 h to form a homogeneous ink. Then, 20  $\mu$ L of the catalyst ink was loaded on one side of a 0.5 × 2 cm<sup>2</sup> graphite paper (loading size was 0.5 × 0.5 cm<sup>2</sup> and sample loading amount was 0.4 mg/cm<sup>2</sup>). The electrode was dried at room temperature. Ag/AgCl (3.5 M KCl) and graphite rod were applied as the reference and counter electrode, respectively. Thirty milliliters of 0.5 M H<sub>2</sub>SO<sub>4</sub> was used as the electrolyte.

Linear sweep voltammetry (LSV) was performed from –0.1 to –0.8 V (vs Ag/AgCl) at 5.0 mV/s. The recorded potentials were calibrated vs the reversible hydrogen electrode (RHE) with the Nernst equation

$$E(\text{vsRHE}) = E(\text{vsAg/AgCl}) + 0.05916 \times \text{pH} + 0.210 \text{ V}$$

The electrochemical impedance spectroscopy (EIS) data were recorded at an overpotential of –0.2 V vs RHE over a frequency ranging from 100 kHz to 0.01 Hz with an amplitude of 0.005 V. Cyclic voltammetry (CV) was done in the range of the non-faradaic region with increasing scan rates (5, 10, 15, 20, 25, and 30 mV/s), and the electrochemical double-layer capacitance ( $C_{\text{dl}}$ ) was equal to the slope of the linear fits at the average potential (0.125 V vs RHE). Generally, the specific capacitance is 20–60  $\mu$ F/cm<sup>2</sup>, and we chose the average value of 40  $\mu$ F/cm<sup>2</sup> to estimate the electrochemical active surface area (ECSA) with the equation

$$\text{ECSA} = \frac{C_{\text{dl}}}{40 \mu\text{F cm}^{-2}} \text{cm}^2$$

**2.4. Computational Details.** First-principles calculations based on DFT<sup>36</sup> were carried out to investigate the mechanism of hydrazine (N<sub>2</sub>H<sub>4</sub>, HZ) doping in 1T- and 2H-MoS<sub>2</sub>. The PBEsol exchange–correlation energy functional<sup>37</sup> was used as it is implemented in the VASP software.<sup>38</sup> The Tkatchenko–Scheffler (TS) dispersion correction method<sup>39</sup> was used to improve the description of van der Waals interaction between the MoS<sub>2</sub> layers.

We used the projector-augmented wave method (PAW)<sup>40</sup> to represent the ionic cores and considered the following electronic states as valence: Mo 4p 5s and 4d; S 2s and 2p; N 2s and 2p; and H 1s. The energy cutoff was set to be 520 eV. A “Hubbard-U” scheme<sup>41</sup> was employed for better treatment of the Mo 3d electric orbitals with a selected  $U$  value of 4.0 eV. For the simulation of the hydrazine-doped systems, we used 8 × 4 × 1 and 4 × 4 × 1 supercells for 1T-MoS<sub>2</sub> (Mo<sub>32</sub>S<sub>64</sub>) and 2H-MoS<sub>2</sub> (Mo<sub>32</sub>S<sub>64</sub>), respectively. For the integrations within the Brillouin zone (BZ), we used a Monkhorst–Pack  $k$ -point grid of 2 × 4 × 8 for the 1T-MoS<sub>2</sub> supercell and of 4 × 4 × 4 for the 2H-MoS<sub>2</sub> supercell. Periodic boundary conditions were applied along the three lattice vectors defining the simulation supercell. Geometry relaxations were performed with a conjugate-

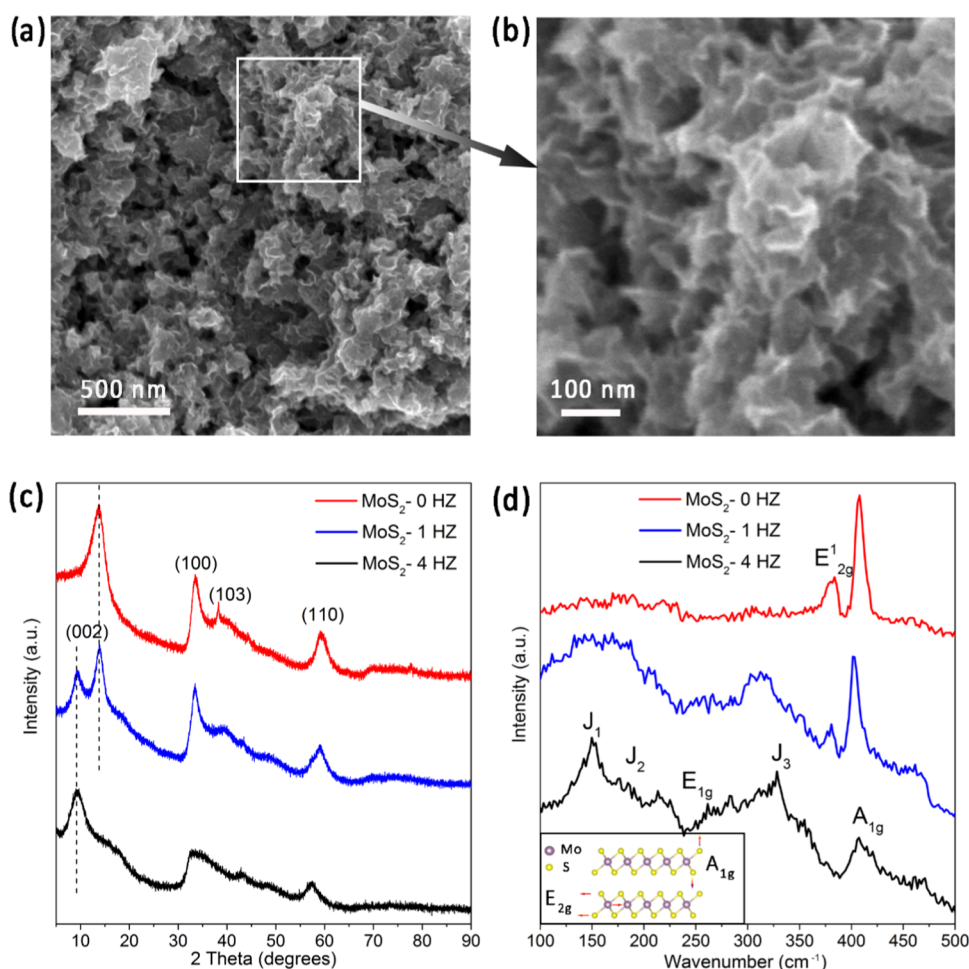


**Figure 1.** (a) SEM images of MoS<sub>2</sub>-4HZ. (b) Zoomed-in image of the square in (a) to show the as-grown nanosheets. (c) XRD pattern showing the shift of (002) peaks of MoS<sub>2</sub>-0HZ, MoS<sub>2</sub>-1HZ, and MoS<sub>2</sub>-4HZ. (d) Raman spectra of MoS<sub>2</sub>-0HZ, MoS<sub>2</sub>-1HZ, and MoS<sub>2</sub>-4HZ. Inset is the schematic diagram of the out-of-plane A<sub>1g</sub> and in-plane E<sub>2g</sub> vibration modes.

gradient algorithm that optimized the ionic positions and the volume and shape of the simulation cell. The relaxations were halted when the forces in the atoms were all below 0.01 eV/Å. By using these technical parameters, total energies were converged to within 0.5 meV per formula unit. Several possible hydrazine intercalation geometries were explored by initializing the structural relaxations from different molecular orientations and the center of the mass sites.

The energy associated with the intercalation of hydrazine molecules between MoS<sub>2</sub> layers ( $E_{\text{intercalation}}$ ) was calculated with the formula

$$E_{\text{intercalation}} = E_{\text{MoS}_2+\text{N}_2\text{H}_4} - E_{\text{MoS}_2} - E_{\text{N}_2\text{H}_4}$$

where  $E_{\text{MoS}_2+\text{N}_2\text{H}_4}$ ,  $E_{\text{MoS}_2}$ , and  $E_{\text{N}_2\text{H}_4}$  stand for the ground-state energy of the hydrazine-intercalated system, pure MoS<sub>2</sub>, and one single hydrazine molecule.

### 3. RESULTS AND DISCUSSION

**3.1. Morphology, Microstructure, and Phase Identification.** All of the MoS<sub>2</sub> samples were synthesized using a hydrothermal method (see the [Material Preparation](#) section for detailed description). To tune the molar ratio of hydrazine monohydrate (N<sub>2</sub>H<sub>4</sub>·H<sub>2</sub>O) to Mo to control the density of interaction, three types of ratios (0:1, 1:1, and 4:1) were adopted to synthesize the MoS<sub>2</sub> at 180 °C for 48 h, and labeled as MoS<sub>2</sub>-0HZ, MoS<sub>2</sub>-1HZ, and MoS<sub>2</sub>-4HZ accordingly. The morphologies of the as-synthesized samples were examined by scanning electron microscopy (SEM). As shown in [Figures 1a](#)

and [S1](#), it is observed from the SEM images that all of the samples are uniformly stacked with the layers of nanosheets. Clearly, there are no observable differences in the macro morphologies of the three types of samples.

To further investigate the effect of reaction temperature on the final products, we set the reaction temperature at 220 °C using identical precursors with the same ratio. It is demonstrated that hydrothermal process at a higher temperature would result in more stacked nanoflowers compared with MoS<sub>2</sub> synthesized without hydrazine (MoS<sub>2</sub>-0HZ-220), while the surface morphology did not change obviously for hydrazine-intercalated samples (MoS<sub>2</sub>-4HZ-220) synthesized under the same conditions ([Figure S2](#)). The possible explanation is that the MoS<sub>2</sub> nanosheets tend to stack more densely under higher temperature and pressure for unintercalated MoS<sub>2</sub>, while the emission of NH<sub>3</sub> gas generated as the byproduct of hydrazine hydrate can compensate for the pressure/strain and thus prevent the nanosheets from densifying the wrapped nanoflowers.<sup>42</sup> The morphology is one of the key factors determining the catalytic properties, and the water-splitting performance of the as-prepared samples with different morphologies will be discussed in the following part.

X-ray diffraction (XRD) measurement was carried out to analyze the crystal structures and lattice parameters. As

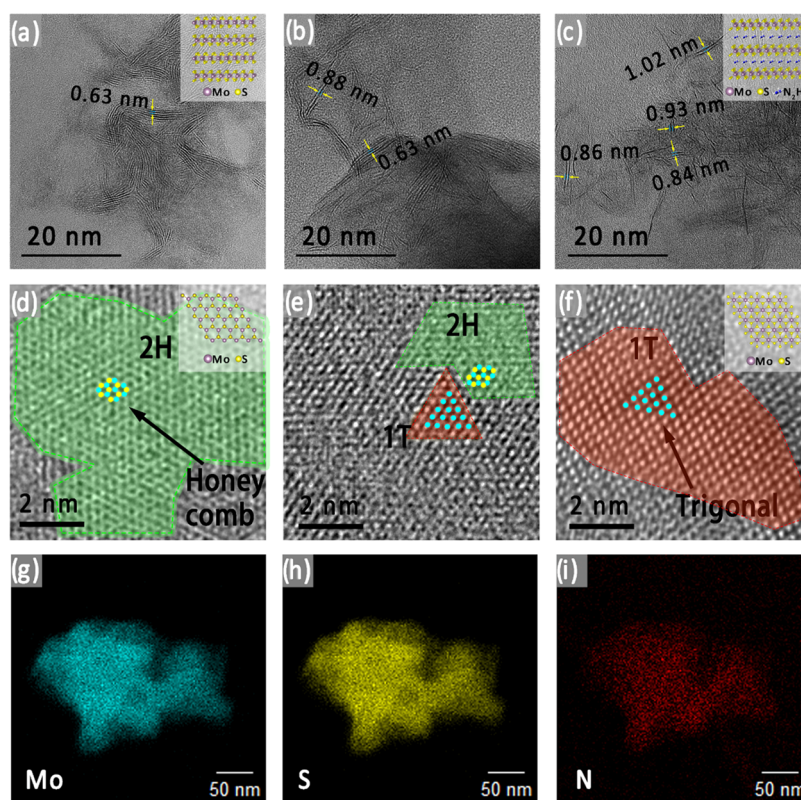


**Figure 2.** (a–c) TEM images of MoS<sub>2</sub>-0HZ, MoS<sub>2</sub>-1HZ, and MoS<sub>2</sub>-4HZ with lattice spacing corresponding to the (002) planes. Insets are the schematic diagrams of 2H- and 1T-MoS<sub>2</sub> from the *a*-axis, respectively. (d–f) High-resolution TEM image of MoS<sub>2</sub>-0HZ, MoS<sub>2</sub>-1HZ, and MoS<sub>2</sub>-4HZ showing the atomic structures of the red-edged region of the 1T (trigonal) phase and green-edged region of 2H (honeycomb) phase. Insets are the schematic diagrams of 2H- and 1T-MoS<sub>2</sub> from the *c*-axis, respectively. (g–i) TEM-EDS mapping of Mo, S, and N elemental distributions of sample MoS<sub>2</sub>-4HZ.

displayed in Figure 1c, the (002) peak of the sample MoS<sub>2</sub>-0HZ is located at the  $2\theta$  angle of  $13.8^\circ$ . For MoS<sub>2</sub>-1HZ, another peak at  $9.2^\circ$  was found. The (002) peak shifting to a lower angle refers to the interlayer lattice expansion.<sup>28</sup> The split peaks of MoS<sub>2</sub>-1HZ indicate that the 1T phase is partially formed as the MoS<sub>2</sub> interlayers are regionally intercalated with hydrazine molecules. For the sample MoS<sub>2</sub>-4HZ, the (002) peak at  $13.8^\circ$  is drastically shifted to  $9.2^\circ$ , which indicates that the interlayers are heavily intercalated with N<sub>2</sub>H<sub>4</sub> molecules, leading to lattice expansion. It should be noted that the wide XRD diffraction peak may suggest the coexistence of two phases,<sup>43,44</sup> and the specific ratio of 1T/2H phase is shown in the XPS analysis later.

The structural phases of the as-made samples were further confirmed by Raman measurements. Figure 1d shows the Raman spectra of the unintercalated MoS<sub>2</sub> and hydrazine-intercalated samples. The sample MoS<sub>2</sub>-4HZ exhibits intense peaks at the wavenumbers of 146, 205, 278, and 325 cm<sup>-1</sup>, representing the J<sub>1</sub>, J<sub>2</sub>, E<sub>1g</sub>, and J<sub>3</sub> Mo-S phonon modes of 1T-phase MoS<sub>2</sub>, respectively.<sup>43,45</sup> The sample MoS<sub>2</sub>-0HZ exhibits strong peaks at the wavenumbers of 382 and 407 cm<sup>-1</sup>, corresponding to the in-plane E<sub>12g</sub> vibration mode (two S atoms directly bound to Mo atoms moving in the same direction and the Mo atom moving in the opposite direction) and the out-of-plane A<sub>1g</sub> vibration mode (S moving in the opposite direction) of MoS<sub>2</sub>, respectively.<sup>46</sup> The relatively integrated intensities of the Raman peaks demonstrate various phases of the samples.<sup>34</sup> The absence of representative 1T-phase peaks in the Raman spectra of sample MoS<sub>2</sub>-0HZ

confirms the pristine semiconductor 2H phase for the unintercalated MoS<sub>2</sub>. As a contrast, the high intensity of the peaks representing the J<sub>1</sub>, J<sub>2</sub>, E<sub>1g</sub>, and J<sub>3</sub> Mo-S phonon modes in the spectra of samples MoS<sub>2</sub>-1HZ and MoS<sub>2</sub>-4HZ verifies the existence of the metallic 1T phase for the hydrazine-intercalated MoS<sub>2</sub>.<sup>8,22</sup> In addition, there was no obvious change in the Raman spectra of the sample MoS<sub>2</sub>-4HZ-220, indicating that the higher synthesis temperature does not lead to phase transformation (Figure S3). Furthermore, no molybdenum oxides or other impurities were detected in the Raman spectra in any samples.

The atomic structure and elemental distribution were characterized by high-resolution transmission electron microscopy (HR-TEM) and energy-dispersive spectroscopy (EDS) measurements. The TEM images as shown in Figure 2a–c clearly show that the MoS<sub>2</sub> nanosheets are formed from several stacked layers via a weak van der Waals interaction for all samples. The average interlayer *d*-spacing of MoS<sub>2</sub>-0HZ is 0.63 nm, corresponding to the (002) lattice plane. As for hydrazine-intercalated MoS<sub>2</sub> (MoS<sub>2</sub>-4HZ), the interlayers have an enlarged *d*-spacing varying from 0.84 to 1.02 nm, indicating the existence of guest species between the layers. The results of the *d*-spacing expansion are consistent with the XRD analysis of 1T-MoS<sub>2</sub> intercalated with Li<sup>+</sup>, K<sup>+</sup>, Na<sup>+</sup>, N, H<sub>2</sub>O, etc.<sup>28,32,43</sup> For the lightly intercalated sample (MoS<sub>2</sub>-1HZ), there is a coexistence of expanded layers (~0.88 nm) and unexpanded layers (0.63 nm). Apart from the difference of interlayer *d*-spacings, the atomic arrangements were examined for phase identification. As illustrated in Figure 2d, the sample MoS<sub>2</sub>-

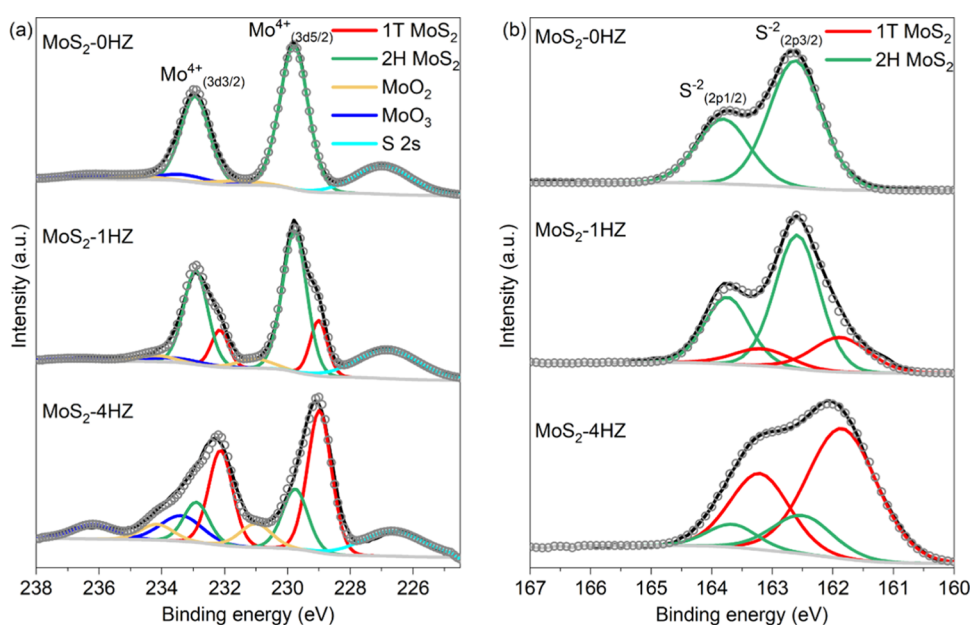


**Figure 3.** XPS spectra associated with (a) Mo (3d) and (b) S (2p) of the sample: (i) MoS<sub>2</sub>-0HZ, (ii) MoS<sub>2</sub>-1HZ, and (iii) MoS<sub>2</sub>-4HZ.

0HZ exhibits a honeycomb atomic arrangement, corresponding to the hexagonal structure of 2H-phase MoS<sub>2</sub>.<sup>9</sup> In Figure 2e, the hydrazine-intercalated sample MoS<sub>2</sub>-4HZ exhibits a trigonal prismatic coordination of Mo atoms, matching well with the 1T-phase MoS<sub>2</sub>.<sup>23,28</sup> Both trigonal and hexagonal atomic alignments are observed in Figure 2f for the lightly intercalated sample MoS<sub>2</sub>-1HZ, indicating the mixed phases of MoS<sub>2</sub>. The elemental distribution was examined by EDS, and the mapping in Figure 2g–i shows the uniform distribution of Mo, S, and N atoms.

The as-prepared MoS<sub>2</sub>-4HZ powder has been stored at ambient conditions for 3 months to test the phase stability, and the peaks representing the 1T phase of MoS<sub>2</sub> are still clearly observed in Raman spectra, endorsing the strong stability of the 1T phase (Figure S4). In contrast to the previously reported unstable 1T-MoS<sub>2</sub> (i.e., quick transformation from the 1T to the 2H phase within 2 h),<sup>34</sup> or the 1T-MoS<sub>2</sub> that only stabilizes as a suspension in the solution,<sup>23</sup> the as-prepared hydrazine-intercalated 1T-phase MoS<sub>2</sub> powder in this work has significantly improved stability at ambient conditions, making it favorable for fabricating reliable and stable catalysts or other TMDs-based devices. Besides, the sample powders were also mixed with DI water to form a homogeneous solution. The uniform black suspension of MoS<sub>2</sub>-4HZ exhibits long-term stability, while the black powders completely precipitated for MoS<sub>2</sub>-0HZ and MoS<sub>2</sub>-1HZ exhibit in-between behavior (Figure S5). The above results demonstrate that the interaction with N<sub>2</sub>H<sub>4</sub> could significantly modify the suspension stability of MoS<sub>2</sub>, matching with the hydrophilicity feature of the 1T phase and the hydrophobicity feature of the 2H phase.<sup>23</sup>

We carried out X-ray photoelectron spectroscopy (XPS) measurements to investigate the composition, valence state, chemical bonding, and the estimated percentage of 1T and 2H phases for each sample. The different electronic states of the 1T and 2H phases would result in the shifts of the Mo (3d) and the S (2p) peaks. It has been reported that the Mo (3d<sub>5/2</sub>) peak of 1T-MoS<sub>2</sub> would shift to binding energies higher by 0.7–1.0 eV relative to the corresponding peak of 2H-MoS<sub>2</sub>,

and the S (2p<sub>3/2</sub>) peak would have a similar shift trend as well.<sup>45</sup> The peak splits are observed in the XPS spectra of sample MoS<sub>2</sub>-1HZ and MoS<sub>2</sub>-4HZ in Figure 3. There are two peaks of Mo<sup>4+</sup> (3d) doublets with the binding energy of 229.1 and 229.8 eV for Mo (3d<sub>5/2</sub>), corresponding to Mo<sup>4+</sup> for 1T and 2H phases, respectively. Similarly, there are two S (2p) doublets with the binding energy of 161.8 and 162.6 eV for S (2p<sub>3/2</sub>), associated with S<sup>2-</sup> for 1T- and 2H-MoS<sub>2</sub>, respectively. Compared to hydrazine-intercalated MoS<sub>2</sub> samples, there is only one Mo (3d<sub>5/2</sub>) peak located at the binding energy of 229.8 eV for MoS<sub>2</sub>-0HZ and also no split of S (2p<sub>3/2</sub>) peak, which suggest the sample is pristine 2H-phase MoS<sub>2</sub>. The peak splits of Mo(3d) and S(2p) indicate that 1T and 2H phases coexist in the hydrazine-incorporated MoS<sub>2</sub>, and the relative proportions of the 1T phase for MoS<sub>2</sub>-0HZ, MoS<sub>2</sub>-1HZ, and MoS<sub>2</sub>-4HZ are estimated to be 0, 22, and 69%, respectively, by the fitting of Mo (3d) core-level spectra. According to the XPS results, it is concluded that an increase in the concentration of hydrazine used in the hydrothermal synthesis of MoS<sub>2</sub> leads to an increasing percentage of the 1T phase, and the as-made MoS<sub>2</sub> becomes 1T-dominant when the molar ratio of N<sub>2</sub>H<sub>4</sub>/Mo is 4:1. The XPS spectra of the sample MoS<sub>2</sub>-4HZ-220 were also examined, and the calculated relative 1T-phase quantification of 70% is fairly consistent with that of MoS<sub>2</sub>-4HZ, indicating that the higher reaction temperature (220 °C compared to 180 °C) does not have an obvious impact on the percentage of 1T phase (Figure S6). It should be noted that the residual oxides MoO<sub>x</sub> may arise from the inevitable surface oxidation during XPS measurement.<sup>47,48</sup> The above XPS results are consistent with the XRD, Raman, and TEM analysis.

To find out the upper limit of the 1T-phase proportion, the sample MoS<sub>2</sub>-12HZ with excess hydrazine in the precursor (molar ratio of N<sub>2</sub>H<sub>4</sub>/Mo = 12:1) was prepared. The XPS results indicate that there is no obvious change in the spectra compared to those of MoS<sub>2</sub>-4HZ (Figure S7). The relative proportion of the 1T phase in MoS<sub>2</sub>-12HZ is calculated to be 70%, which is very close to that of MoS<sub>2</sub>-4HZ (69%). Based on the XPS analysis, it can be concluded that the molar ratio of N<sub>2</sub>H<sub>4</sub>/Mo = 4:1 already reaches the limitation and the excess

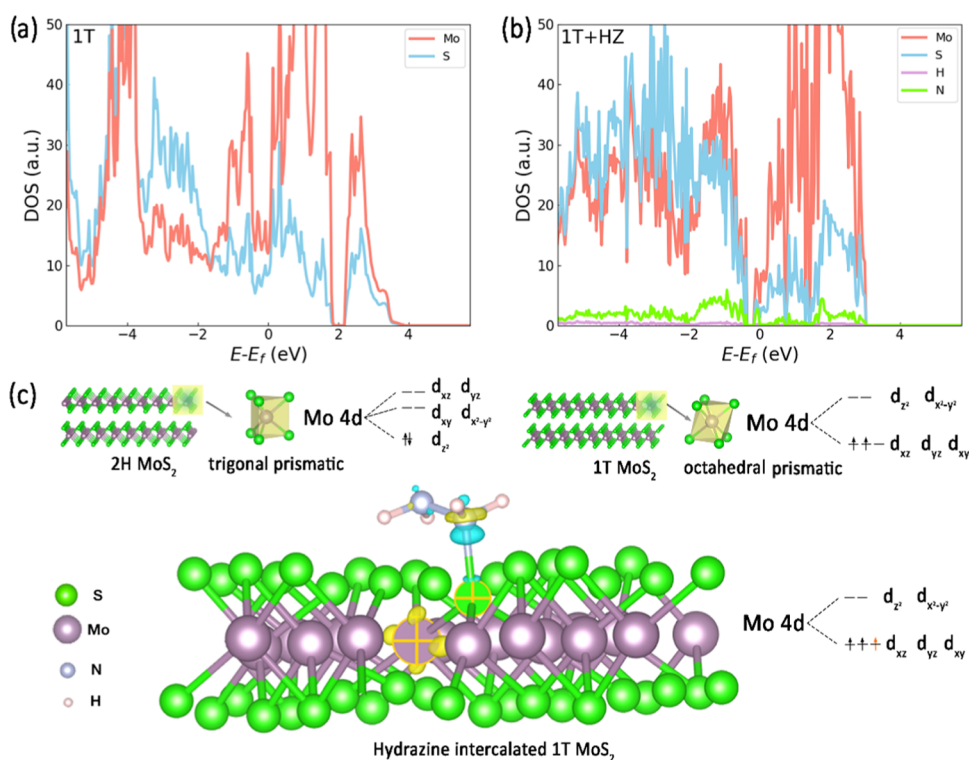


**Figure 4.** Density of state (DOS) for each element of (a) 1T-MoS<sub>2</sub> and (b) 1T-MoS<sub>2</sub> + HZ. The DOS of N and H are scaled to a factor of 7.5 for better visualization. The Fermi energy ( $E_f$ ) has been shifted to zero ( $E - E_f = 0$ ). (c) Schematics of the Mo 4d orbitals of 2H-MoS<sub>2</sub>, 1T-MoS<sub>2</sub>, and 1T-MoS<sub>2</sub> + HZ. Specifically, the charge density difference of 1T-MoS<sub>2</sub> with HZ intercalation, and accumulation and depletion spaces are revealed in blue and yellow, respectively. The atoms involved in the formation of the N–S bond and accompanying electronic charge redistribution processes in MoS<sub>2</sub> are highlighted with crosses. The isosurface value is 0.025 e/Å<sup>3</sup>.

hydrazine hydrate does not lead to a higher percentage of the 1T phase. In addition, the doublets representing N (1s) are shown in Figure S8. The peaks at 402.1 and 399.6 eV are assigned to the binding energies of N linked to MoS<sub>2</sub> (electron donor) and the distal N in N<sub>2</sub>H<sub>4</sub>, respectively.<sup>49</sup> Besides, the XPS analysis based on the survey scan indicates that the quantification of N increases with the increased feed ratio of N<sub>2</sub>H<sub>4</sub>, and the molar ratio of Mo to S atoms is approximately 1:2, agreeing well with the nominal quantification for all of the samples (Figure S9 and Table S1).

**3.2. Mechanism Study.** To investigate the hydrazine intercalation mechanism in 1T- and 2H-MoS<sub>2</sub> at the atomistic scale, we performed first-principles calculations based on DFT (see the Computational Details section for the technical description of the DFT calculations). The equilibrium geometries deriving from our theoretical calculations are shown in Figure 4. It can be appreciated that a bond is created between one N atom in the hydrazine molecule and one S atom in MoS<sub>2</sub> for the 1T polymorph but not for 2H (Figure S10). By explicitly calculating the hydrazine intercalation energy  $E_{\text{intercalation}}$ , we found that the introduction of N<sub>2</sub>H<sub>4</sub> molecules between the MoS<sub>2</sub> layers is an exothermic process for the 1T polymorph, whereas it is endothermic for 2H. In particular, we obtained  $E_{\text{intercalation}}$  values for the intercalation of N<sub>2</sub>H<sub>4</sub> as  $-6.117$  eV for 1T-MoS<sub>2</sub> and  $1.541$  eV for 2H-MoS<sub>2</sub> (Table S2). In consistent agreement with the experiments, the DFT results indicate that upon N<sub>2</sub>H<sub>4</sub> doping, the 1T polymorph is stabilized over 2H-MoS<sub>2</sub> since the intercalation of N<sub>2</sub>H<sub>4</sub> molecules in 1T-MoS<sub>2</sub> is energetically favorable (i.e.,  $E_{\text{intercalation}} < 0$ ) in contrast to 2H-MoS<sub>2</sub> (i.e.,  $E_{\text{intercalation}} > 0$ ).

To understand the electronic origins of our DFT  $E_{\text{intercalation}}$  results, we performed a detailed analysis of the electronic density of states (DOS) and charge distribution in the doped and undoped MoS<sub>2</sub> polymorphs. The partial DOS values for doped and pristine 1T- and 2H-MoS<sub>2</sub> are shown in Figures 4, S11, and S12. First, the electronic band structure of the 1T polymorph changes significantly upon N<sub>2</sub>H<sub>4</sub> doping, whereas that of the 2H polymorph does not, indicating the presence of strong (weak) molecule–MoS<sub>2</sub> interactions in the former (latter) case (in agreement with the bond formation sketched in Figure 4 and mentioned above). For instance, the small energy band gap observed at approximately 2 eV above the Fermi level for pristine 1T-MoS<sub>2</sub> is shifted down to roughly  $-0.1$  eV in N<sub>2</sub>H<sub>4</sub>-doped 1T-MoS<sub>2</sub>, and the density of Mo and S electronic states around the Fermi level changes appreciably. Second, the energy region in the valence band over which the electronic states of the N<sub>2</sub>H<sub>4</sub> molecule and MoS<sub>2</sub> overlap is much broader for the 1T polymorph than for 2H (i.e., of several eV in the former case and of the order of 0.1 eV in the latter case). These results are fully consistent with our  $E_{\text{intercalation}}$  results.

To further study the interplay between MoS<sub>2</sub> and hydrazine, Bader charge calculations were performed to analyze how electronic charges are redistributed among the hydrazine molecule and the 1T-MoS<sub>2</sub> polymorph as a result of the N–S bond formation. Our DFT Bader charge analysis indicates that a Mo docking position gets reduced with an approximate negative charge of 0.1 e<sup>-</sup>, which mainly comes from the N<sub>2</sub>H<sub>4</sub> molecule. The S atom forming the bond with hydrazine appears to act as a charge bridge between the Mo ion and the molecule since its net charge does not change appreciably (see

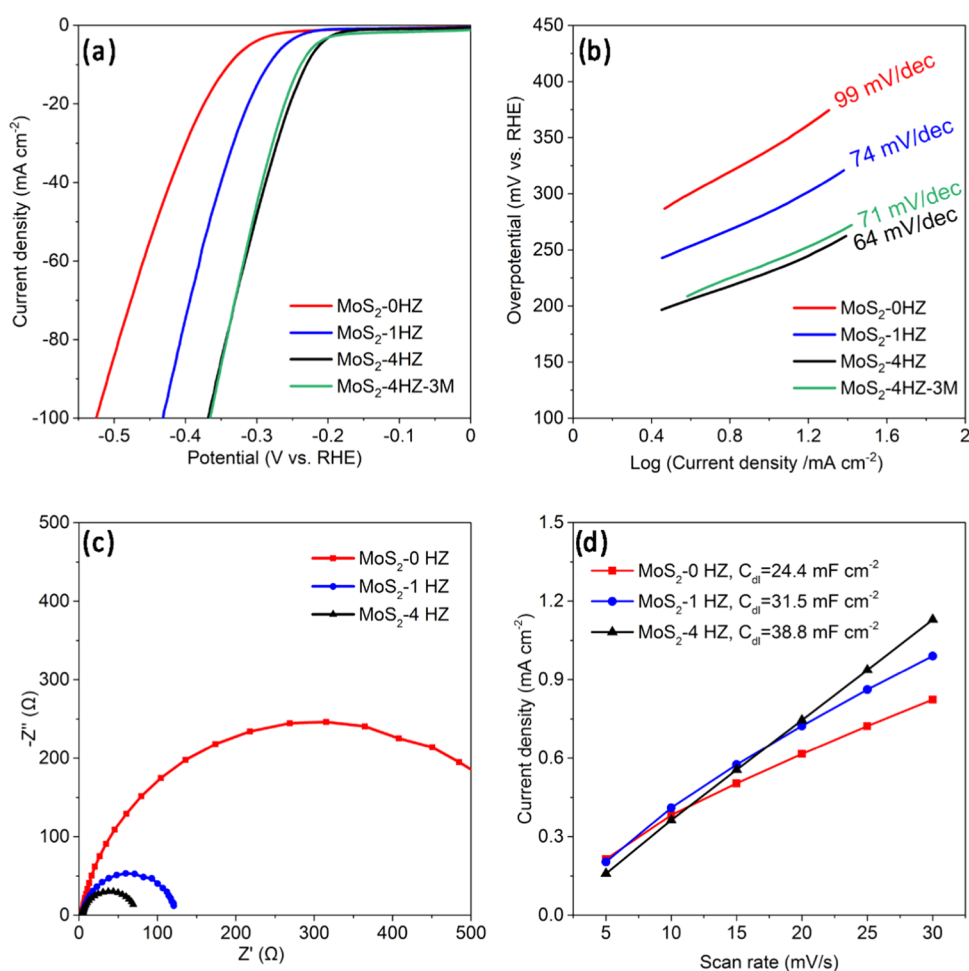


**Figure 5.** (a) HER LSV polarization curves in 0.5 M H<sub>2</sub>SO<sub>4</sub> solution; (b) corresponding Tafel slopes derived from LSV; (c) EIS measurement; and (d) linear fitting plots of the electrochemical double-layer capacitance ( $C_{dl}$ ) calculated from the CV test in the non-faradaic region at scan rates of 5, 10, 15, 20, 25, and 30 mV/s.

the charge density difference plot in Figure 4c). Moreover, it is known that the degeneracy and occupation of Mo 4d orbitals in 1T- and 2H-phase MoS<sub>2</sub> are different. Specifically, the 4d<sub>z<sup>2</sup></sub> orbitals are fully occupied in the stable semiconductive 2H phase, while the 4d<sub>xy,yz,xz</sub> are partially occupied in the metastable metallic phase.<sup>31,50</sup> It has been reported that the stability of 1T-MoS<sub>2</sub> could be enhanced by alkali metal intercalation, such as Li<sup>+</sup> and K<sup>+</sup>, which offers additional electrons to half fill the 4d<sub>xy,yz,xz</sub> orbitals.<sup>7,32</sup> Based on our Bader charge analysis, we propose that the electron donation by the hydrazine molecules has a similar thermal stability-enhancing effect in 1T-MoS<sub>2</sub>.

**3.3. Electrical Conductivity and Electrocatalytic Properties.** The four-point-probe method was applied to test the electrical conductivity of the samples. The loose sample powders were compressed to form dense thin pellets for measurement as illustrated in Figure S13, and the sheet resistance was plotted to demonstrate the conductivity in Figure S14 and Table S3. The sheet resistance is as high as 28.9 kΩ/square for the pristine 2H-phase MoS<sub>2</sub>-0HZ, but dramatically decreases to 41.1 Ω/square for the 1T-dominant MoS<sub>2</sub>-4HZ, verifying the metallic behavior of the 1T phase. According to the DFT calculations, the intercalated hydrazine molecules provide electrons and thus greatly increase the carrier concentration, leading to enhanced electrical conductivity.

The electrocatalytic performance of the HER was evaluated by electrochemical measurements. As illustrated in the linear sweep voltammetry (LSV) curves in Figure 5a, the HER performance is improved with an increased proportion of the 1T phase. The onset potential is reduced from 286 to 242 to 196 mV vs RHE for samples MoS<sub>2</sub>-0HZ, MoS<sub>2</sub>-1HZ, and MoS<sub>2</sub>-4HZ, respectively. Similarly, the derived Tafel slope in Figure 5b decreased from 99 to 74 to 64 mV/dec, implying the accelerated kinetics of the electrocatalytic reaction. Apart from these, the electrocatalytic property of sample MoS<sub>2</sub>-4HZ-3M was also tested (Figure 5a,b). After being exposed to ambient conditions for 3 months, the as-prepared sample still exhibits outstanding stability with a similar LSV curve to the freshly made sample MoS<sub>2</sub>-4HZ, which further confirms the neglectable 1T-phase degradation for a long period at room temperature. The HER process involves multiple steps in an acidic solution: (i) discharge reaction (Volmer), H<sub>3</sub>O<sup>+</sup> + e<sup>-</sup> = H<sub>ads</sub> + H<sub>2</sub>O; (ii) electrochemical desorption reaction (Heyrovsky), H<sub>ads</sub> + H<sub>3</sub>O<sup>+</sup> + e<sup>-</sup> = H<sub>2</sub> + H<sub>2</sub>O; and (iii) combination reaction (Tafel), H<sub>ads</sub> + H<sub>ads</sub> = H<sub>2</sub>.<sup>13</sup> The HER mechanism of the edge Mo sites of 2H-MoS<sub>2</sub> and the basal plane of 1T-MoS<sub>2</sub> have both been reported to follow the Volmer–Heyrovsky steps with the respective rate-limiting step of the electrochemical desorption reaction.<sup>12,20</sup> Compared to the pristine 2H-MoS<sub>2</sub> (MoS<sub>2</sub>-0HZ), the decreased Tafel slope indicates that the catalytic performance of the 1T-dominant

MoS<sub>2</sub> (MoS<sub>2</sub>-4HZ) follows the Volmer–Heyrovsky mechanism, and the HER reaction is promoted by the rate-limiting Heyrovsky reaction.

The enhancement of HER performance is also associated with improved electrical conductivity and rich active sites. 1T-MoS<sub>2</sub> possesses a relatively high carrier concentration and better electrical conductivity, which benefit charge transfer, while 2H-MoS<sub>2</sub> shows reduced conductivity; thus the charge transfer kinetics is then restrained. The electrochemical impedance spectroscopy (EIS) measurement in Figure 5c reveals that the 1T-dominant MoS<sub>2</sub> has lower resistance, confirming the facilitation of electron transfer and enhancement of HER performance. Besides, the active sites for hydrogen absorption for 2H-MoS<sub>2</sub> are limited to Mo edge sites, while there are more active sites for 1T-MoS<sub>2</sub> due to the moderate hydrogen binding energy of S atoms on the basal plane.<sup>12,20</sup> The electrochemical active surface area (ECSA) value generally represents the number of active sites for hydrogen evolution, and it is calculated by the C<sub>d</sub> derived from the cyclic voltammetry (CV) scans in the non-faradaic region with increasing scan rates (Figures 5d and S15). The ECSA has an increasing trend (609.62, 787.23, and 970.66 cm<sup>2</sup>) with a higher proportion of the 1T phase (0, 22, and 69%), demonstrating more active sites in the sample MoS<sub>2</sub>-4HZ for HER. The HER performances of the three samples are summarized in Table S4.

It should be mentioned that the above samples were synthesized at 180 °C during the hydrothermal process. To compare the effect of synthesis temperature on the HER performance, the LSV curves of samples MoS<sub>2</sub>-0HZ-220 and MoS<sub>2</sub>-4HZ-220 are plotted in Figure S16. The increased synthesis temperature does not affect the HER performance of the 1T-dominant MoS<sub>2</sub>-4HZ obviously, while the catalytic property shows an observable drop for the 2H-phase MoS<sub>2</sub>-0HZ with an elevated synthesis temperature. As discussed in the previous part, the hydrothermal process at the higher temperature would result in more stacked nanoflowers when MoS<sub>2</sub> was synthesized without hydrazine (MoS<sub>2</sub>-0HZ), while the morphology remains similar for hydrazine-intercalated samples (MoS<sub>2</sub>-4HZ). Thus, the performance changes accordingly. Therefore, there is a correlation between the HER performance of MoS<sub>2</sub> with the surface morphology, and the densely wrapped nanoflowers are unfavorable for the water-splitting performance compared to the loosely stacked nanosheets, which could be explained by the higher surface contact area with the electrolyte for loosely stacked nanosheets.

#### 4. CONCLUSIONS

In this work, a one-step hydrothermal method has been developed to precisely control the 2H/1T-phase abundance in MoS<sub>2</sub> through the intercalation of hydrazine molecules, serving as electron donors. The morphology, atomic structures, chemical bonding, and phase quantification have been carefully examined and characterized. The as-synthesized 1T-dominant MoS<sub>2</sub> nanosheets exhibit significantly improved HER performance as a result of a synergistic combination of accelerated kinetics, reduced resistance, and increase of active sites, which makes MoS<sub>2</sub> competitive for prospective industrial uses as a catalyst for high-efficient water splitting. Moreover, the as-synthesized sample shows superior phase stability at ambient conditions owing to the intercalation of hydrazine molecules, thus eliminating the thermodynamic instabilities of 1T-MoS<sub>2</sub>.

In addition, DFT calculations show that the stabilization of the metallic phase can be attributed to the electron donation from the intercalated N<sub>2</sub>H<sub>4</sub> molecules to the adjacent Mo atoms. This work has demonstrated a simple yet effective approach to synthesize highly stable 1T-MoS<sub>2</sub> nanosheets with precise phase control, which may provide key strategies in the fabrication of advanced 2D TMDs catalysts and devices.

#### ■ ASSOCIATED CONTENT

##### SI Supporting Information

The Supporting Information is available free of charge at <https://pubs.acs.org/doi/10.1021/acsami.2c02675>.

SEM images of MoS<sub>2</sub>-0HZ and MoS<sub>2</sub>-1HZ (Figure S1); SEM images of MoS<sub>2</sub>-4HZ-220 and MoS<sub>2</sub>-0HZ-220 (Figure S2); Raman spectra of MoS<sub>2</sub>-4HZ-220 (Figure S3); Raman spectra of MoS<sub>2</sub>-4HZ-3M (Figure S4); images of solutions (Figure S5); XPS spectra of MoS<sub>2</sub>-4HZ-220 (Figure S6); XPS spectra of MoS<sub>2</sub>-12HZ (Figure S7); XPS spectra associated with N (1s) (Figure S8); XPS survey scans (Figure S9); structures of 1T-MoS<sub>2</sub> + N<sub>2</sub>H<sub>4</sub> and 2H-MoS<sub>2</sub> + N<sub>2</sub>H<sub>4</sub> (Figure S10); zoomed-in DOS of 1T-MoS<sub>2</sub> + HZ (Figure S11); DOS of 2H-MoS<sub>2</sub> and 2H-MoS<sub>2</sub> + HZ (Figure S12); MoS<sub>2</sub> pellets (Figure S13); sheet resistance of sample pellets (Figure S14); CV curves (Figure S15); LSV curves of MoS<sub>2</sub>-0HZ-220 and MoS<sub>2</sub>-4HZ-220 (Figure S16); atomic ratio identified by XPS measurement (Table S1); ground-state energy and intercalation energy (Table S2); sheet resistance (Table S3); summary of HER performance (Table S4) (PDF)

#### ■ AUTHOR INFORMATION

##### Corresponding Authors

Tao Wan – School of Materials Science and Engineering, University of New South Wales, Sydney, NSW 2052, Australia; [orcid.org/0000-0001-9345-8624](https://orcid.org/0000-0001-9345-8624); Email: [tao.wan@unsw.edu.au](mailto:tao.wan@unsw.edu.au)

Claudio Cazorla – Department de Física, University Politècnica de Catalunya, Barcelona 08034, Spain; [orcid.org/0000-0002-6501-4513](https://orcid.org/0000-0002-6501-4513); Email: [claudio.cazorla@upc.edu](mailto:claudio.cazorla@upc.edu)

Jiabao Yi – Global Innovative Centre for Advanced Nanomaterials, College of Engineering, Science and Environment, The University of Newcastle, Callaghan, NSW 2308, Australia; [orcid.org/0000-0001-5299-9897](https://orcid.org/0000-0001-5299-9897); Email: [jiabao.yi@newcastle.edu.au](mailto:jiabao.yi@newcastle.edu.au)

##### Authors

Mengyao Li – School of Materials Science and Engineering, University of New South Wales, Sydney, NSW 2052, Australia

Zizhen Zhou – School of Materials Science and Engineering, University of New South Wales, Sydney, NSW 2052, Australia

Long Hu – School of Engineering, Macquarie University Sustainable Energy Research Centre, Macquarie University, Sydney, NSW 2109, Australia

Shuangyue Wang – School of Materials Science and Engineering, University of New South Wales, Sydney, NSW 2052, Australia

**Yingze Zhou** – School of Materials Science and Engineering, University of New South Wales, Sydney, NSW 2052, Australia

**Renbo Zhu** – School of Materials Science and Engineering, University of New South Wales, Sydney, NSW 2052, Australia

**Xueze Chu** – Global Innovative Centre for Advanced Nanomaterials, College of Engineering, Science and Environment, The University of Newcastle, Callaghan, NSW 2308, Australia

**Ajayan Vinu** – Global Innovative Centre for Advanced Nanomaterials, College of Engineering, Science and Environment, The University of Newcastle, Callaghan, NSW 2308, Australia; [orcid.org/0000-0002-7508-251X](https://orcid.org/0000-0002-7508-251X)

**Dewei Chu** – School of Materials Science and Engineering, University of New South Wales, Sydney, NSW 2052, Australia; [orcid.org/0000-0003-4581-0560](https://orcid.org/0000-0003-4581-0560)

Complete contact information is available at:  
<https://pubs.acs.org/10.1021/acsami.2c02675>

## Notes

The authors declare no competing financial interest.

## ACKNOWLEDGMENTS

J.Y. acknowledges the financial support by the ARC Future Fellowship (FT160100205). D.C. acknowledges the financial support by the ARC Discovery Project (DP210100879). C.C. acknowledges the support from the Spanish Ministry of Science, Innovation and Universities under the “Ramón y Cajal” fellowship RYC2018-024947-I.

## REFERENCES

- (1) Ahmed, S.; Yi, J. Two-Dimensional Transition Metal Dichalcogenides and Their Charge Carrier Mobilities in Field-Effect Transistors. *Nano-Micro Lett.* **2017**, *9*, No. 50.
- (2) Chaudhary, N.; Khanuja, M.; Abid; Islam, S. S. Hydrothermal Synthesis of MoS<sub>2</sub> Nanosheets for Multiple Wavelength Optical Sensing Applications. *Sens. Actuators, A* **2018**, *277*, 190–198.
- (3) Furlan, K. P.; de Mello, J. D. B.; Klein, A. N. Self-Lubricating Composites Containing MoS<sub>2</sub>: A Review. *Tribol. Int.* **2018**, *120*, 280–298.
- (4) Ahmed, S.; Ding, X.; Bao, N.; Bian, P.; Zheng, R.; Wang, Y.; Murmu, P. P.; Kennedy, J. V.; Liu, R.; Fan, H.; Suzuki, K.; Ding, J.; Yi, J. Inducing High Coercivity in MoS<sub>2</sub> Nanosheets by Transition Element Doping. *Chem. Mater.* **2017**, *29*, 9066–9074.
- (5) Kou, Z.; Wang, K.; Liu, Z.; Zeng, L.; Li, Z.; Yang, B.; Lei, L.; Yuan, C.; Hou, Y. Recent Advances in Manifold Exfoliated Synthesis of Two-Dimensional Non-Precious Metal-Based Nanosheet Electrocatalysts for Water Splitting. *Small Struct.* **2022**, *3*, No. 2100153.
- (6) Liu, K.-H.; Zhong, H.-X.; Li, S.-J.; Duan, Y.-X.; Shi, M.-M.; Zhang, X.-B.; Yan, J.-M.; Jiang, Q. Advanced Catalysts for Sustainable Hydrogen Generation and Storage via Hydrogen Evolution and Carbon Dioxide/Nitrogen Reduction Reactions. *Prog. Mater. Sci.* **2018**, *92*, 64–111.
- (7) Fang, Y.; Pan, J.; He, J.; Luo, R.; Wang, D.; Che, X.; Bu, K.; Zhao, W.; Liu, P.; Mu, G.; Zhang, H.; Lin, T.; Huang, F. Structure Redetermination and Superconductivity Observation of Bulk 1T MoS<sub>2</sub>. *Angew. Chem., Int. Ed.* **2018**, *57*, 1232–1235.
- (8) Tan, S. J. R.; Abdelwahab, I.; Ding, Z.; Zhao, X.; Yang, T.; Loke, G. Z. J.; Lin, H.; Verzhbitskiy, I.; Poh, S. M.; Xu, H.; Nai, C. T.; Zhou, W.; Eda, G.; Jia, B.; Loh, K. P. Chemical Stabilization of 1T' Phase Transition Metal Dichalcogenides with Giant Optical Kerr Non-linearity. *J. Am. Chem. Soc.* **2017**, *139*, 2504–2511.
- (9) Coleman, J. N.; Lotya, M.; O'Neill, A.; Bergin, S. D.; King, P. J.; Khan, U.; Young, K.; Gaucher, A.; De, S.; Smith, R. J.; Shvets, I. V.;

Arora, S. K.; Stanton, G.; Kim, H.-Y.; Lee, K.; Kim, G. T.; Duesberg, G. S.; Hallam, T.; Boland, J. J.; Wang, J. J.; Donegan, J. F.; Grunlan, J. C.; Moriarty, G.; Shmeliov, A.; Nicholls, R. J.; Perkins, J. M.; Grievson, E. M.; Theuwissen, K.; McComb, D. W.; Nellist, P. D.; Nicolosi, V. Two-Dimensional Nanosheets Produced by Liquid Exfoliation of Layered Materials. *Science* **2011**, *331*, 568–571.

(10) Coutinho, S. S.; Tavares, M. S.; Barboza, C. A.; Frazão, N. F.; Moreira, E.; Azevedo, D. L. 3R and 2H Polytypes of MoS<sub>2</sub>: DFT and DFPT Calculations of Structural, Optoelectronic, Vibrational and Thermodynamic Properties. *J. Phys. Chem. Solids* **2017**, *111*, 25–33.

(11) Barua, S.; Dutta, H. S.; Gogoi, S.; Devi, R.; Khan, R. Nanostructured MoS<sub>2</sub>-Based Advanced Biosensors: A Review. *ACS Appl. Nano Mater.* **2018**, *1*, 2–25.

(12) Jaramillo, T. F.; Jørgensen, K. P.; Bonde, J.; Nielsen, J. H.; Horch, S.; Chorkendorff, I. Identification of Active Edge Sites for Electrochemical H<sub>2</sub> Evolution from MoS<sub>2</sub> Nanocatalysts. *Science* **2007**, *317*, 100–102.

(13) Huang, Y.; Nielsen, R. J.; William, A.; Goddard, I.; Soriaga, M. P.; et al. The Reaction Mechanism with Free Energy Barriers for Electrochemical Dihydrogen Evolution on MoS<sub>2</sub>. *J. Am. Chem. Soc.* **2015**, *137*, 6692–6698.

(14) Tsai, C.; Chan, K.; Nørskov, J. K.; Abild-Pedersen, F. Theoretical Insights Into the Hydrogen Evolution Activity of Layered Transition Metal Dichalcogenides. *Surf. Sci.* **2015**, *640*, 133–140.

(15) Youn, D. H.; Han, S.; Kim, J. Y.; Kim, J. Y.; Park, H.; Choi, S. H.; Lee, J. S. Highly Active and Stable Hydrogen Evolution Electrocatalysts Based on Molybdenum Compounds on Carbon Nanotube–Graphene Hybrid Support. *ACS Nano* **2014**, *8*, 5164–5173.

(16) Li, F.; Zhang, L.; Li, J.; Lin, X.; Li, X.; Fang, Y.; Huang, J.; Li, W.; Tian, M.; Jin, J.; Li, R. Synthesis of Cu–MoS<sub>2</sub>/rGO Hybrid as Non-noble Metal Electrocatalysts for the Hydrogen Evolution Reaction. *J. Power Sources* **2015**, *292*, 15–22.

(17) Lei, Z.; Zhan, J.; Tang, L.; Zhang, Y.; Wang, Y. Recent Development of Metallic (1T) Phase of Molybdenum Disulfide for Energy Conversion and Storage. *Adv. Energy Mater.* **2018**, *8*, No. 1703482.

(18) Meng, F.; Zhong, H.; Bao, D.; Yan, J.; Zhang, X. In Situ Coupling of Strung Co<sub>4</sub>N and Intertwined N–C Fibers toward Free-Standing Bifunctional Cathode for Robust, Efficient, and Flexible Zn–Air Batteries. *J. Am. Chem. Soc.* **2016**, *138*, 10226–10231.

(19) Zhong, H.; Liu, K.; Zhang, Q.; Meng, F.; Bao, D.; Zhang, X. Copper Tetraxolate Based Metal–Organic Frameworks as Highly Efficient Catalysts for Artificially Chemical and Electrochemical CO<sub>2</sub> Conversion. *Nano Select* **2020**, *1*, 311–319.

(20) Tang, Q.; Jiang, D.-e. Mechanism of Hydrogen Evolution Reaction on 1T-MoS<sub>2</sub> from First Principles. *ACS Catal.* **2016**, *6*, 4953–4961.

(21) Liu, Q.; Fang, Q.; Chu, W.; Wan, Y.; Li, X.; Xu, W.; Habib, M.; Tao, S.; Zhou, Y.; Liu, D.; Xiang, T.; Khalil, A.; Wu, X.; Chhowalla, M.; Ajayan, P. M.; Song, L. Electron-Doped 1T-MoS<sub>2</sub> via Interface Engineering for Enhanced Electrocatalytic Hydrogen Evolution. *Chem. Mater.* **2017**, *29*, 4738–4744.

(22) Lukowski, M. A.; Daniel, A. S.; Meng, F.; Forticaux, A.; Li, L.; Jin, S. Enhanced Hydrogen Evolution Catalysis from Chemically Exfoliated Metallic MoS<sub>2</sub> Nanosheets. *J. Am. Chem. Soc.* **2013**, *135*, 10274–10277.

(23) Geng, X.; Sun, W.; Wu, W.; Chen, B.; Al-Hilo, A.; Benamara, M.; Zhu, H.; Watanabe, F.; Cui, J.; Chen, T.-p. Pure and Stable Metallic Phase Molybdenum Disulfide Nanosheets for Hydrogen Evolution Reaction. *Nat. Commun.* **2016**, *7*, No. 10672.

(24) Li, M.; Cai, B.; Tian, R.; Yu, X.; Breese, M. B. H.; Chu, X.; Han, Z.; Li, S.; Joshi, R.; Vinu, A.; Wan, T.; Ao, Z.; Yi, J.; Chu, D. Vanadium Doped 1T MoS<sub>2</sub> Nanosheets for Highly Efficient Electrocatalytic Hydrogen Evolution in both Acidic and Alkaline Solutions. *Chem. Eng. J.* **2021**, *409*, No. 128158.

(25) Li, H.; Tsai, C.; Koh, A. L.; Cai, L.; Contryman, A. W.; Frapapan, A. H.; Zhao, J.; Han, H. S.; Manoharan, H. C.; Abild-Pedersen, F.; Nørskov, J. K.; Zheng, X. Activating and Optimizing

MoS<sub>2</sub> Basal Planes for Hydrogen Evolution Through the Formation of Strained Sulphur Vacancies. *Nat. Mater.* **2016**, *15*, 48–53.

(26) Hu, J.; Zhang, C.; Zhang, Y.; Yang, B.; Qi, Q.; Sun, M.; Zi, F.; Leung, M. K. H.; Huang, B. Interface Modulation of MoS<sub>2</sub>/Metal Oxide Heterostructures for Efficient Hydrogen Evolution Electrocatalysis. *Small* **2020**, *16*, No. 2002212.

(27) Yin, Y.; Han, J.; Zhang, Y.; Zhang, X.; Xu, P.; Yuan, Q.; Samad, L.; Wang, X.; Wang, Y.; Zhang, Z.; Zhang, P.; Cao, X.; Song, B.; Jin, S. Contributions of Phase, Sulfur Vacancies, and Edges to the Hydrogen Evolution Reaction Catalytic Activity of Porous Molybdenum Disulfide Nanosheets. *J. Am. Chem. Soc.* **2016**, *138*, 7965–7972.

(28) Acerce, M.; Voiry, D.; Chhowalla, M. Metallic 1T Phase MoS<sub>2</sub> Nanosheets as Supercapacitor Electrode Materials. *Nat. Nanotechnol.* **2015**, *10*, 313–318.

(29) Voiry, D.; Goswami, A.; Kappera, R.; e Silva, C. D. C. C.; Kaplan, D.; Fujita, T.; Chen, M.; Asefa, T.; Chhowalla, M. Covalent Functionalization of Monolayered Transition Metal Dichalcogenides by Phase Engineering. *Nat. Chem.* **2015**, *7*, 45–49.

(30) Geng, X.; Zhang, Y.; Han, Y.; Li, J.; Yang, L.; Benamara, M.; Chen, L.; Zhu, H. Two-Dimensional Water-Coupled Metallic MoS<sub>2</sub> with Nanochannels for Ultrafast Supercapacitors. *Nano Lett.* **2017**, *17*, 1825–1832.

(31) Enyashin, A. N.; Yadgarov, L.; Houben, L.; Popov, I.; Weidenbach, M.; Tenne, R.; Bar-Sadan, M.; Seifert, G. New Route for Stabilization of 1T-WS<sub>2</sub> and MoS<sub>2</sub> Phases. *J. Phys. Chem. C* **2011**, *115*, 24586–24591.

(32) Park, S.; Kim, C.; Park, S. O.; Oh, N. K.; Kim, U.; Lee, J.; Seo, J.; Yang, Y.; Lim, H. Y.; Kwak, S. K.; Kim, G.; Park, H. Phase Engineering of Transition Metal Dichalcogenides with Unprecedentedly High Phase Purity, Stability, and Scalability via Molten-Metal-Assisted Intercalation. *Adv. Mater.* **2020**, *32*, No. 2001889.

(33) Wypych, F.; Schöllhorn, R. 1T-MoS<sub>2</sub>, a New Metallic Modification of Molybdenum Disulfide. *J. Chem. Soc., Chem. Commun.* **1992**, *21*, 1386–1388.

(34) Yang, D.; Sandoval, S. J.; Divigalpitiya, W. M. R.; Irwin, J. C.; Frindt, R. F. Structure of Single-Molecular-Layer MoS<sub>2</sub>. *Phys. Rev. B* **1991**, *43*, 12053–12056.

(35) Duerloo, K.-A. N.; Li, Y.; Reed, E. J. Structural Phase Transitions in Two-Dimensional Mo- and W-Dichalcogenide Monolayers. *Nat. Commun.* **2014**, *5*, No. 4214.

(36) Cazorla, C.; Boronat, J. Simulation and Understanding of Atomic and Molecular Quantum Crystals. *Rev. Mod. Phys.* **2017**, *89*, No. 035003.

(37) Perdew, J. P.; Ruzsinszky, A.; Csonka, G. I.; Vydrov, O. A.; Scuseria, G. E.; Constantin, L. A.; Zhou, X.; Burke, K. Restoring the Density-Gradient Expansion for Exchange in Solids and Surfaces. *Phys. Rev. Lett.* **2008**, *100*, No. 136406.

(38) Kresse, G.; Furthmüller, J. Efficient Iterative Schemes for ab Initio Total-Energy Calculations Using a Plane-Wave Basis set. *Phys. Rev. B* **1996**, *54*, No. 11169.

(39) Tkatchenko, A.; Scheffler, M. Accurate Molecular Van der Waals Interactions From Ground-State Electron Density and Free-Atom Reference Data. *Phys. Rev. Lett.* **2009**, *102*, No. 073005.

(40) Blöchl, P. E. Projector Augmented-Wave Method. *Phys. Rev. B* **1994**, *50*, No. 17953.

(41) Dudarev, S.; Botton, G.; Savrasov, S.; Humphreys, C.; Sutton, A. Electron-Energy-Loss Spectra and the Structural Stability of Nickel Oxide: An LSDA + U Study. *Phys. Rev. B* **1998**, *57*, No. 1505.

(42) Li, H.; Chen, S.; Jia, X.; Xu, B.; Lin, H.; Yang, H.; Song, L.; Wang, X. Amorphous Nickel-Cobalt Complexes Hybridized With 1T-Phase Molybdenum Disulfide via Hydrazine-Induced Phase Transformation for Water Splitting. *Nat. Commun.* **2017**, *8*, No. 15377.

(43) Liu, Q.; Li, X.; He, Q.; Khalil, A.; Liu, D.; Xiang, T.; Wu, X.; Song, L. Gram-Scale Aqueous Synthesis of Stable Few-Layered 1T-MoS<sub>2</sub>: Applications for Visible-Light-Driven Photocatalytic Hydrogen Evolution. *Small* **2015**, *11*, 5556–5564.

(44) Wu, K.; Cao, X.; Li, M.; Lei, B.; Zhan, J.; Wu, M. Bottom-Up Synthesis of MoS<sub>2</sub>/CNTs Hollow Polyhedron with 1T/2H Hybrid

Phase for Superior Potassium-Ion Storage. *Small* **2020**, *16*, No. 2004178.

(45) Fan, X.; Xu, P.; Zhou, D.; Sun, Y.; Li, Y. C.; Nguyen, M. A. T.; Terrones, M.; Mallouk, T. E. Fast and Efficient Preparation of Exfoliated 2H MoS<sub>2</sub> Nanosheets by Sonication-Assisted Lithium Intercalation and Infrared Laser-Induced 1T to 2H Phase Reversion. *Nano Lett.* **2015**, *15*, 5956–5960.

(46) Wang, S.; Huang, J.-K.; Li, M.; Azam, A.; Zu, X.; Qiao, L.; Yang, J.; Li, S. Growth of High-Quality Monolayer Transition Metal Dichalcogenide Nanocrystals by Chemical Vapor Deposition and Their Photoluminescence and Electrocatalytic Properties. *ACS Appl. Mater. Interfaces* **2021**, *13*, 47962–47971.

(47) Knirsch, K. C.; Berner, N. C.; Nerl, H. C.; Cucinotta, C. S.; Gholamvand, Z.; McEvoy, N.; Wang, Z.; Abramovic, I.; Vecera, P.; Halik, M.; Sanvito, S.; Duesberg, G. S.; Nicolosi, V.; Hauke, F.; Hirsch, A.; Coleman, J. N.; Backes, C. Basal-Plane Functionalization of Chemically Exfoliated Molybdenum Disulfide by Diazonium Salts. *ACS Nano* **2015**, *9*, 6018–6030.

(48) Gatensby, R.; McEvoy, N.; Lee, K.; Hallam, T.; Berner, N. C.; Rezvani, E.; Winters, S.; O'Brien, M.; Duesberg, G. S. Controlled Synthesis of Transition Metal Dichalcogenide Thin Films for Electronic Applications. *Appl. Surf. Sci.* **2014**, *297*, 139–146.

(49) Liu, Z.; Ou, J.; Wang, H.; You, X.; Ye, M. Synthesis and Characterization of Hydrazide-Linked and Amide-Linked Organic Polymers. *ACS Appl. Mater. Interfaces* **2016**, *8*, 32060–32067.

(50) Huang, Q.; Li, X.; Sun, M.; Zhang, L.; Song, C.; Zhu, L.; Chen, P.; Xu, Z.; Wang, W.; Bai, X. The Mechanistic Insights into the 2H-1T Phase Transition of MoS<sub>2</sub> upon Alkali Metal Intercalation: From the Study of Dynamic Sodiation Processes of MoS<sub>2</sub> Nanosheets. *Adv. Mater. Interfaces* **2017**, *4*, No. 1700171.